



**HAL**  
open science

## New U-Pb zircon and $^{40}\text{Ar}/^{39}\text{Ar}$ muscovite age constraints on the emplacement of the Lizio syn-tectonic granite (Armorican Massif, France)

Romain Tartese, Marc Poujol, Gilles Ruffet, Philippe Boulvais, Philippe Yamato, Jan Kosler

### ► To cite this version:

Romain Tartese, Marc Poujol, Gilles Ruffet, Philippe Boulvais, Philippe Yamato, et al.. New U-Pb zircon and  $^{40}\text{Ar}/^{39}\text{Ar}$  muscovite age constraints on the emplacement of the Lizio syn-tectonic granite (Armorican Massif, France). *Comptes Rendus Géoscience*, 2011, 343 (7), pp.443-453. 10.1016/j.crte.2011.07.005 . insu-00624529

**HAL Id: insu-00624529**

**<https://insu.hal.science/insu-00624529>**

Submitted on 19 Sep 2011

**HAL** is a multi-disciplinary open access archive for the deposit and dissemination of scientific research documents, whether they are published or not. The documents may come from teaching and research institutions in France or abroad, or from public or private research centers.

L'archive ouverte pluridisciplinaire **HAL**, est destinée au dépôt et à la diffusion de documents scientifiques de niveau recherche, publiés ou non, émanant des établissements d'enseignement et de recherche français ou étrangers, des laboratoires publics ou privés.

1 New U-Pb zircon and  $^{40}\text{Ar}/^{39}\text{Ar}$  muscovite age constraints on the emplacement  
2 of the Lizio syn-tectonic granite (Armorican Massif, France)

3

4 Nouveaux âges U-Pb sur zircon et  $^{40}\text{Ar}/^{39}\text{Ar}$  sur muscovite de mise en place du  
5 granite syn-tectonique de Lizio (Massif Armoricain, France)

6

7 **Romain Tartèse<sup>1\*</sup>, Marc Poujol<sup>1</sup>, Gilles Ruffet<sup>1,2</sup>, Philippe Boulvais<sup>1</sup>, Philippe Yamato<sup>1</sup>,**  
8 **Jan Košler<sup>3</sup>**

9

10 <sup>1</sup>UMR CNRS 6118 Géosciences, Université de Rennes 1, 35042 Rennes Cedex, France

11 <sup>2</sup>CNRS (CNRS/INSU) UMR 6118, Géosciences Rennes, 35042 Rennes Cedex, France

12 <sup>3</sup>Department of Earth Science and Centre for Geobiology, University of Bergen, N-5007  
13 Bergen, Norway

14

15 \*Corresponding author: R. Tartèse (romain.tartese@univ-rennes1.fr)

16 Phone: 0033 2 23 23 30 81

17 Fax: 0033 2 23 23 60 97

18

19

20

21

22

23

24

25

26 **Abstract**

27 LA-ICP-MS U-Pb analyses performed on zircon grains from the Lizio granite yielded an  
28 emplacement age of  $316 \pm 6$  Ma. Typical S-C structures show that the Lizio granite was  
29 emplaced contemporaneously with dextral shearing along the northern branch of the South  
30 Armorican Shear Zone and that it was therefore active at that time.  $^{40}\text{Ar}/^{39}\text{Ar}$  analyses  
31 performed on muscovite grains yielded plateau dates ranging between 311.5 and 308.2 Ma.  
32 Muscovite chemistry is typical of primary magmatic muscovite, which precludes a late fluids-  
33 induced resetting of the K-Ar isotopic system.  $^{40}\text{Ar}/^{39}\text{Ar}$  dates thus likely correspond to the  
34 cooling ages below the argon closure temperature. Considering the uncertainties on the  
35 measured ages, we can propose that either the Lizio granite cooled down quickly in less than a  
36 million of years or that it remained in a hot environment for several millions of years after its  
37 emplacement. This latter scenario could have been sustained by shear heating during dextral  
38 shearing along the northern branch of the South Armorican Shear Zone.

39

40 **Résumé**

41 Les analyses U-Pb réalisées sur des zircons du granite de Lizio par LA-ICP-MS ont livré un  
42 âge de mise en place de  $316 \pm 6$  Ma. Des structures C-S caractéristiques démontrent que le  
43 granite de Lizio s'est mis en place pendant le cisaillement dextre le long de la branche nord du  
44 Cisaillement Sud Armoricain, qui était donc toujours actif à cette époque. Les analyses  
45  $^{40}\text{Ar}/^{39}\text{Ar}$  réalisées sur les muscovites ont donné des âges plateaux allant de 311.5 à 308.2 Ma.  
46 La chimie des muscovites est typique de celle d'une muscovite magmatique primaire, ce qui  
47 écarte une remise à zéro tardive, induite par des fluides, du système isotopique K-Ar. Ces  
48 dates  $^{40}\text{Ar}/^{39}\text{Ar}$  correspondent donc probablement à des âges de refroidissement sous la  
49 température de fermeture de l'argon. En tenant compte des incertitudes sur les âges obtenus,  
50 cela implique soit un refroidissement rapide du granite de Lizio en moins d'un million

51 d'années soit qu'il est resté dans un environnement chaud pendant plusieurs millions d'années  
52 après sa mise en place, grâce à la chaleur frictionnelle produite pendant le cisaillement dextre  
53 le long du Cisaillement Sud Armoricaïn.

54

55 **Keywords**

56  $^{40}\text{Ar}/^{39}\text{Ar}$  dating; Armoricaïn Massif; Lizio granite; South Armoricaïn Shear Zone; U-Pb dating

57 **Mots-clés**

58 Datation  $^{40}\text{Ar}/^{39}\text{Ar}$ ; Massif Armoricaïn; Granite de Lizio; Cisaillement Sud Armoricaïn;

59 Datation U-Pb

60

61

62

63

64

65

66

67

68

69

70

71

72

73

74

75

## 76 **1. Introduction**

77 In the continental crust, granitic plutons emplace at different stages during the  
78 evolution of an orogen. In the Armorican Variscan belt, numerous peraluminous granites were  
79 emplaced during the Carboniferous (e.g. Bernard-Griffiths et al., 1985). Most of these granites  
80 are spatially associated with the dextral lithospheric-scale South Armorican Shear Zone.  
81 Moreover, emplacement of these granites is often coeval with shearing as indicated by the S-  
82 C structures they display (Berthé et al., 1979; Gapais, 1989). The precise dating of these  
83 synkinematic granites and of their cooling history is therefore an essential tool to place time  
84 constraints on the different tectono-thermal events that occur during the life of the Variscan  
85 orogen.

86 So far, available geochronological data on the emplacement of these granites are  
87 solely provided by whole rock Rb-Sr isochron ages (Bernard-Griffiths et al., 1985; Peucat et  
88 al., 1979). Along the northern branch of the South Armorican Shear Zone, three granitic  
89 massifs are assumed to have emplaced synkinematically around  $344\text{-}337 \pm 13\text{-}8$  Ma, which  
90 implies that the shear zone was active during the Lower Viséan. In order to better constrain  
91 dextral shearing along the northern branch of the South Armorican Shear Zone, we have  
92 performed new zircon U-Pb and muscovite  $^{40}\text{Ar}/^{39}\text{Ar}$  datings.

93

## 94 **2. Geological framework**

95 During Variscan times, the Armorican Massif has undergone deformation related to a  
96 major continental collision between Gondwana and Laurussia (e.g. Ballèvre et al., 2009). This  
97 episode was followed by the development of dextral shear zones that can be traced over a  
98 distance of a couple of hundred of kilometres, namely the North Armorican Shear Zone  
99 (NASZ) and the South Armorican Shear Zone (SASZ) (Fig. 1a). The SASZ separates two  
100 distinct domains within the Armorican Massif that are characterized by contrasted

101 metamorphic and structural histories. To the South, the south Armorican domain (SAD) is  
102 mainly composed of deep crustal units (medium to high-grade micaschists, migmatitic  
103 gneisses and anatectic granites) that have been exhumed during the extension associated with  
104 the chain collapse (e.g. Brown and Dallmeyer, 1996; Gapais et al., 1993; Turrillot et al.,  
105 2009). To the North, the central Armorican domain (CAD) is made of a late Proterozoic –  
106 early Palaeozoic sedimentary succession, which has been affected by low-grade  
107 metamorphism (e.g. Le Corre et al., 1991). In the CAD, both strain intensity (Gumiaux et al.,  
108 2004), metamorphic degree (Le Corre et al., 1991) and evidence of fluid flow (Gloaguen et  
109 al., 2007; Lemarchand et al., 2011) increase southward reaching a maximum on the SASZ  
110 itself.

111 The SASZ is geometrically defined by ca. 100-1000m wide zone of highly strained  
112 mylonitic rocks (Jégouzo, 1980; Tartèse et al., 2011a). In details, the SASZ is divided into  
113 two main branches (Fig. 1a). In the southern branch network (SBSASZ), the mylonitic  
114 foliation bears a 5-10° eastward dipping stretching lineation. Along this branch, a dextral  
115 displacement of ca. 150 to 200 km has been proposed based on the width of the mylonitized  
116 rocks (Jégouzo and Rossello, 1988). The northern branch (NBSASZ) is sub-linear and  
117 extends for about 300 km. It displays a subvertical mylonitic foliation also bearing a  
118 stretching lineation dipping at ca. 10° eastward. Along this branch, a 40 km minimal dextral  
119 offset has been estimated from geometrical reconstructions (Jégouzo and Rossello, 1988).

120 The Lizio two-mica granite was emplaced along the NBSASZ (Fig. 1b). This granitic  
121 massif is highly emblematic because it represents the *locus typicus* where S-C structures were  
122 first described as resulting from a single deformational event (Berthé et al., 1979). These  
123 structures indicate that the Lizio granite was emplaced during shearing along the NBSASZ.  
124 Indeed, “S-planes” correspond to shearing planes which localized the dextral deformation.  
125 These “S-planes” are vertical and their orientation mimics that of the NBSASZ. “C-planes”

126 correspond to cleavage planes. These “C-planes” rotate during non-coaxial shearing. They  
127 define an angle of around 45° with “S-planes” in slightly deformed samples, angle which  
128 decreases with increasing strain until parallelisation of “S-planes” and “C-planes” in  
129 ultramytonitized samples (Berthé et al., 1979). According to Gapais (1989), these S-C  
130 structures developed during cooling of intrusives at temperatures around 550°C. The  
131 synkinematic characteristics of the Lizio granite emplacement is also evidenced by the triple-  
132 point defined by the foliation around the intrusion (Fig. 2). This triple-point formed by the  
133 combination of the regional stress and the stress related to the granite emplacement.

134         Whole rock Rb-Sr data obtained on the Lizio granite define a  $338 \pm 13$  Ma isochron  
135 age ( $2\sigma$ ) interpreted as the granite emplacement age (Peucat et al., 1979). This age is similar  
136 within error to the  $344 \pm 8$  Ma and  $337 \pm 13$  Ma ages ( $2\sigma$ ) obtained by these authors on the  
137 Pontivy and Bignan synkinematic massifs, both located a couple of kilometres westward and  
138 also rooted into the NBSASZ (Fig. 1b). More recently, a zircon U-Pb emplacement age of  $316$   
139  $\pm 5/-3$  Ma (ID-TIMS, Béchenec et al., 2001) has been obtained on the St-Thurien metagranite  
140 ca. 250 m south of the NBSASZ ( $3^{\circ}40'23''$ W;  $47^{\circ}57'50''$ N). This St-Thurien metagranite is  
141 highly sheared and displays characteristics S-C structures, with subvertical “S-planes” and  
142 “C-planes” oriented N105-110° and ca. N080°, respectively (Béchenec et al., 2001). The St-  
143 Thurien metagranite is thus synkinematic with dextral shearing along the NBSASZ, which  
144 indicates that shearing continued after 330-325 Ma.

145         The geochemistry of the Lizio two-mica granite has been studied in details by Tartèse  
146 and Boulvais (2010). This study provided mineral and whole rock geochemical data as well as  
147 new Rb-Sr, Sm-Nd and O isotope data which are consistent with the few data published by  
148 Bernard-Griffiths et al. (1985). The Lizio granite is highly silicic, poor in ferro-magnesian and  
149 was formed by partial melting of a metasedimentary source. Geochemical data show that a  
150 subtle magmatic differentiation occurred by crystal fractionation from the melt (Tartèse and

151 Boulvais, 2010). Finally the Lizio granite intruded Brioverian metapelites of the CAD. During  
152 its emplacement in the Brioverian metapelites, a syntectonic paragenesis of Bt + Ms + Chl +  
153 St + Grt ± And developed (Berthé, 1980; mineral abbreviations are after Whitney and Evans,  
154 2010), corresponding to the facies 2b of Pattison and Tracy (1991) and to a pressure of around  
155 4 kbar (Pattison et al., 1999).

156

### 157 **3. Samples description**

#### 158 *3.1. Petrography*

159 A full petrographic description of the samples presented in this study, as well as  
160 mineral and whole-rock geochemical data, and oxygen isotope data are given in Tartèse and  
161 Boulvais (2010). To summarize, in the Lizio two-mica granite, quartz and feldspar  
162 (orthoclase, microcline and plagioclase) represent around 90% of the mineral assemblage  
163 (Fig. 3) while biotite and muscovite represent the remaining 10%, biotite being generally  
164 more abundant than muscovite. Accessory minerals are apatite, zircon and monazite.

165 In undeformed samples, quartz is large and often euhedral (Fig. 3a-b) whereas it is  
166 recrystallized in ribbons in deformed samples (Fig. 3c-d). Plagioclase is euhedral to sub-  
167 euhedral and shows thin polysynthetic twinning. Alkali feldspar is generally sub-euhedral.  
168 Microcline and orthoclase generally displays well-expressed tartan and Carlsbad twinning,  
169 respectively. Pleochroic biotite forms euhedral brown-reddish flakes (Fig. 3a-b) and hosts  
170 most of the accessory minerals (Fig. 3b). Muscovite usually forms large flakes, some of them  
171 having a fish-like habit due to shearing (Fig. 3c). In deformed samples, shear bands are  
172 usually localized in small biotite and muscovite grains aggregates (Fig. 3c-d).

173

#### 174 *3.2. Mineral chemistry*

175 Analytical procedure for electron microprobe analysis of minerals are detailed in Pitra  
176 et al. (2008) and Tartèse and Boulvais (2010). K-feldspar is close to the orthose end-member  
177 (Or = 91-92 mol.%) and plagioclase is albite on average (Ab = 91 mol.%). Biotite  
178 composition is homogeneous in the investigated samples and typical of peraluminous granites  
179 (Tartèse and Boulvais, 2010). Concerning muscovite, complementary electron microprobe  
180 data have been acquired, compared to the dataset published in Tartèse and Boulvais (2010), as  
181 muscovite is the mineral chosen for  $^{40}\text{Ar}/^{39}\text{Ar}$  dating in this study. Only data obtained on large  
182 muscovite phenocrysts are reported in Table 1 and displayed in Fig. 4. Muscovite grains have  
183 a homogeneous chemical composition with FeO = 1.1-1.4 wt.%, MgO = 0.8-0.9 wt.% and  
184 Na<sub>2</sub>O = 0.5-0.7 wt.% (Table 1). They also have a high TiO<sub>2</sub> content (0.6-1.1 wt.% on average,  
185 Table 1) and consistently fall in the primary magmatic muscovite field in the Mg-Ti-Na  
186 ternary diagram (Miller et al., 1981; Fig. 4a). In the Mg + Fe against Si plot (Fig. 4b),  
187 muscovite analyses are clustered showing that limited phengitic substitution occurred in the  
188 studied samples.

189

## 190 **4. Geochronological results**

### 191 *4.1. Zircon U-Pb dating*

192 Zircon U-Pb data were obtained *in-situ* by laser ablation inductively coupled plasma  
193 mass spectrometry (LA-ICP-MS) performed at the Centre for Element and Isotope Analysis,  
194 University of Bergen, Norway. A classical mineral separation procedure has been followed to  
195 concentrate zircon grains suitable for U-Pb dating from samples LRT10, LRT12 and LRT15,  
196 these three samples representing undeformed, deformed and mylonitized end-members in the  
197 rock collection. Rocks were crushed and the powder fractions with a diameter < 250 µm have  
198 been isolated. Heavy minerals were successively concentrated by Wilfley table and heavy  
199 liquids procedures. Magnetic minerals were then removed with an isodynamic Frantz

200 separator. Zircon grains were carefully examined under a binocular microscope, selected, and  
201 embedded in epoxy mounts. Then grains were hand-grounded and polished on a lap wheel  
202 with 6  $\mu\text{m}$  and 1  $\mu\text{m}$  diamond suspension successively. They were imaged in transmitted and  
203 reflected light, and their internal structure has been revealed using SEM BSE imaging at the  
204 LaSalle Institute, Beauvais, France.

205 Before analysis, grain mounts were cleaned using a weak  $\text{HNO}_3$  solution and rinsed  
206 several times using Millipore water and ethanol in an ultrasonic bath. They were then  
207 mounted in the laser ablation cell together with several standards for quality control. A  $^{213}\text{Nd}$ -YAG  
208 laser (New Wave UP-213) was used coupled to a single-collector, double focusing  
209 magnetic sector ICP-MS system (Thermo Finnigan Element 2). Data have been plotted in  
210 Wetherill concordia diagrams using the software Isoplot/Ex (Ludwig, 2008). In Fig. 5, data  
211 are plotted with their uncertainties at  $1\sigma$ . Results are reported in the Table 2 where  
212 uncertainties are listed at  $1\sigma$ . When ages are calculated, all errors are reported at the  
213  $2\sigma$  confidence level.

214 Zircon grains were ablated using a laser beam of ca. 15  $\mu\text{m}$  in diameter that was  
215 rastered over the sample surface to create a line of ca. 50  $\mu\text{m}$  in length depending on the grain  
216 size. The laser energy was set at 5  $\text{J}\cdot\text{cm}^{-2}$  with a repetition rate of 10 Hz. Together with the  
217 sample introduction, the system allowed the simultaneous nebulization of an internal standard  
218 tracer solution following the technique described by Košler et al. (2002) and Košler &  
219 Sylvester (2003). Zircon data were collected on unknown zircon grains and three zircon  
220 standards, 91500 (1065 Ma; Wiedenbeck et al., 1995), Plešovice (337 Ma; Sláma et al., 2008)  
221 and GJ-1 (609 Ma; Jackson et al., 2004). Typically 10-15 unknowns were collected for every  
222 7 analyses of the standards. Analysing and treating the zircon standards as unknowns is a  
223 robust quality control procedure that allows assessment of the accuracy and precision of the  
224 technique during an analytical session. Analyses done on the Plešovice and GJ-1 zircon

225 standards yielded concordant ages of  $335 \pm 4$  Ma ( $n = 12$ ; MSWD = 1.13) and  $603 \pm 11$  Ma ( $n$   
226 = 9; MSWD = 0.30). Raw data were processed off-line using an Excel spreadsheet-based  
227 program (Lamdate; Košler et al., 2008).

228 BSE images of zircon grains from sample LRT12 revealed unzoned grey cores  
229 surrounded by thin darker rims, without evidence of inherited cores (Fig. 5d). In sample  
230 LRT15, zircon grains display a more pronounced oscillatory zoning where dark cores are  
231 surrounded by brighter rims (Fig. 5d). Some zircon grains also contain small monazite  
232 inclusions (for example in LRT15-Zirc3 in Fig. 5d). In sample LRT10, two analyses are  
233 largely discordant and yield therefore meaningless dates (Fig. 5a). From the remaining  
234 concordant analyses, one yields a date of ca. 950 Ma and another five dates are grouped  
235 around 600-500 Ma (Fig. 5a). In sample LRT15, the complete dataset of 11 analyses plot in a  
236 concordant to sub-concordant position (Fig. 5b). Among them, six define an imprecise  
237 concordia age of  $319 \pm 15$  Ma (MSWD = 0.23). The five remaining datapoints define dates  
238 between ca. 600 and 450 Ma. Finally, in sample LRT12, eleven analyses have been performed  
239 (Table 2). When plotted in a Wetherill concordia diagram (Fig. 5c), nine datapoints define a  
240 concordia age of  $316.4 \pm 5.6$  Ma (MSWD = 0.64), identical within error with the age recorded  
241 by sample LRT15 but more precise.

242

#### 243 4.2. *Muscovite $^{40}\text{Ar}/^{39}\text{Ar}$ dating*

244 Euhedral to subeuhedral single grains of muscovite, with variably deformed shapes,  
245 were handpicked from the 0.25-1.50 mm fraction. Irradiation was performed at the McMaster  
246 reactor (Hamilton, Canada) and lasted 43.33 hr (total fluence of  $2.6 \times 10^{18}$  n.cm<sup>-2</sup>). It was  
247 monitored with Taylor Creek Rhyolite (TCR-2) sanidine (28.34 Ma, Renne et al. 1998).  
248 Muscovite single grains were analyzed by step-heating with a  $^{40}\text{Ar}/^{39}\text{Ar}$  laser probe, following  
249 the procedure described in Ruffet et al. (1991; 1995). Blanks were performed routinely each

250 first or third step, and subtracted from subsequent sample gas fractions. A plateau age is  
251 obtained when apparent ages of at least three consecutive steps, representing a minimum of  
252 70% of the  $^{39}\text{Ar}$  released, agree within  $2\sigma$  error bars with the integrated age of the plateau  
253 segment. The  $^{40}\text{Ar}/^{39}\text{Ar}$  analytical data are portrayed as age spectra in Fig. 6. All reported  
254 uncertainties both in the Fig. 6 and in the text are at the  $2\sigma$  confidence level.

255         Single muscovite grains have been analyzed in four samples from the Lizio granite  
256 (LRT10, LRT11, LRT13 and LRT15). These samples yielded plateau dates ranging between  
257  $311.5 \pm 0.4$  Ma down to  $308.2 \pm 0.6$  Ma (Fig. 6). They display slight saddle-shaped  $^{40}\text{Ar}/^{39}\text{Ar}$   
258 age spectra that might reflect slight perturbations of the K-Ar isotopic system (e.g.  
259 Alexandrov et al., 2002; Cheilletz et al., 1999). An important point is that there is no  
260 relationship between the obtained dates and the shearing gradient observed throughout the  
261 Lizio granite.

262

## 263         **5. Interpretation and discussion**

264         Considering the high closure temperature for the U-Pb radiogenic system in zircon in  
265 excess of  $800^\circ\text{C}$  (Cherniak and Watson, 2001), we interpret the age of  $316 \pm 6$  Ma obtained  
266 on sample LRT12 from the synkinematic Lizio granite as its emplacement age along the  
267 NBSASZ. The age of  $319 \pm 15$  Ma obtained on sample LRT15 is imprecise but consistent  
268 with this emplacement age. Older dates obtained on zircon grains from samples LRT10 and  
269 LRT15 illustrate the classical phenomenon of inheritance which often characterizes granitic  
270 rocks (e.g. Bea et al., 2007; Harrison et al., 1987; Miller et al., 2003; Roddick & Bevier,  
271 1995). Here, inherited dates mainly range between Neo-Proterozoic and Upper Ordovician  
272 times. Concerning the emplacement age of  $316 \pm 6$  Ma, it is identical to the zircon U-Pb  
273 emplacement age of  $316 +5/-3$  Ma of the St-Thurien metagranite found by B  chenec et al.  
274 (2001) and contemporaneous with dextral shearing along the NBSASZ. It is also identical to

275 the U-Pb zircon emplacement age obtained recently on the southward Questembert granite by  
276 Tartèse et al. (2011b), which is contemporaneous with dextral shearing along the SBSASZ.  
277 This new U-Pb emplacement age obtained on the Lizio granite thus indicates that both  
278 branches of the SASZ were active at the same time around 315-320 Ma. However, it is  
279 younger and does not overlap with the whole rock Rb-Sr isochron age of  $337 \pm 13$  Ma ( $2\sigma$ ),  
280 previously considered as the emplacement age of the granite (Whole rock Rb-Sr isochron,  
281 recalculated from the six data of Peucat et al., 1979 and the three data of Tartèse and  
282 Boulvais, 2010). So far, all the available geochronological data imply that the NBSASZ has  
283 been active from ca. 344 Ma (whole rock Rb-Sr isochron age of the Pontivy granite, Peucat et  
284 al., 1979) down to ca. 315 Ma. However, it would be interesting to get new zircon U-Pb data  
285 on the other granitic massifs emplaced along the NBSASZ. Indeed, the existing Rb-Sr  
286 isochron ages may be too old for these granites. Such old inherited “isochrons” have been  
287 described for example by Roddick and Compston (1977) for the crustally-derived  
288 Murrumbidgee Batholith, Australia. Moreover, whole rock-mineral isochrons on two samples  
289 from the Pontivy granite (whole rock Rb-Sr isochron age of  $344 \pm 8$  Ma) yielded ages  
290 identical within error at  $311 \pm 9$  and  $310 \pm 9$  Ma respectively (Peucat et al., 1979), ages that  
291 are consistent with a Late Carboniferous emplacement for the Pontivy granite. We thus  
292 believe that the ca. 340 Ma old emplacement ages obtained through whole rock Rb-Sr dating  
293 of synkinematic granites along the NBSASZ are actually not emplacement ages of these  
294 granites but rather represent inherited “isochrons” in the sense of Roddick and Compston  
295 (1977). In that case, initiation of dextral shearing along the NBSASZ may not be as old as the  
296 ca. 340 Ma age that has been considered so far. Indeed, our data on the Lizio granite give a  
297 maximum age of 322 Ma for the activity along the NBSASZ.

298  $^{40}\text{Ar}/^{39}\text{Ar}$  dates obtained on muscovite grains from four samples of the Lizio granite  
299 range between 311.5 and 308.2 Ma. The two oldest dates are identical within error with the

300 zircon U-Pb emplacement age of  $316 \pm 6$  Ma and involve a sub-instantaneous cooling of the  
301 intrusion, and the two other dates are slightly younger, considering the uncertainties  
302 associated with both techniques. This implies that either the younger muscovite grains have  
303 been affected by fluid-induced recrystallization processes after their magmatic isotopic  
304 closure (e.g. Villa, 2010) which would have reset the  $^{40}\text{Ar}/^{39}\text{Ar}$  dates, or that the Lizio granite  
305 remained sufficiently warm during 2-3 Ma after its emplacement, above the argon closure  
306 temperature of muscovite. The muscovite chemistry shows that all the muscovite grains have  
307 a typical primary magmatic composition, which likely precludes the first hypothesis of a  
308 fluids-induced recrystallization and resetting process. The closure temperature for argon in  
309 muscovite has for a long time been considered to be around  $350^\circ\text{C}$  based in part on calibration  
310 of obtained ages vs. metamorphic grade (e.g. Purdy and Jäger, 1976). However, Harrison et  
311 al. (2009) recently published the first experimental study of argon diffusion in muscovite and  
312 showed that Ar retentivity in muscovite is greater than previously assumed. Based on their  
313 diffusion parameters ( $E_a = 264 \text{ kJ}\cdot\text{mol}^{-1}$ ;  $D_0 = 2.3\text{E}^{-04} \text{ m}^2\cdot\text{s}^{-1}$ ), and taking 500 and 1000  $\mu\text{m}$  for  
314 the diffusion radius, we have computed the different closure temperature as a function of  
315 cooling rates (Fig. 7a): the closure temperature ranges between ca.  $450$  and  $550^\circ\text{C}$ , for the  
316 diffusion dimensions and cooling rates investigated. In a Temperature-Time diagram (Fig.  
317 7b), the minimum cooling rate calculated considering U-Pb and  $^{40}\text{Ar}/^{39}\text{Ar}$  ages and their  
318 associated uncertainties is  $10.4^\circ\text{C}/\text{Ma}$ .

319         Taking the minimum zircon U-Pb age and the oldest muscovite dates corresponds to a  
320 sub-instantaneous cooling of the granitic body. A simple 2D thermal numerical model (details  
321 in Appendix A) shows that a Lizio-type granitic pluton emplaced at mid-crustal depths cools  
322 down in less than 1 Ma (Fig. 8), consistently with this scenario. Conversely, a slow cooling  
323 rate of ca.  $10^\circ\text{C}/\text{Ma}$  would imply that the Lizio granite remained at a temperature above ca.  
324  $480\text{-}500^\circ\text{C}$  for a long time after its emplacement. The Lizio granite was emplaced around 4

325 kbar, which corresponds to a depth of 15 km considering only the lithostatic pressure and a  
326 granite density of 2.7. At this depth, temperatures of around 550°C can be reached and  
327 maintained along continental strike-slip shear zones due to heat production by shear heating  
328 (Leloup et al., 1999). The cooling below the closure temperature of ca. 500°C for such a slow  
329 cooling rate would have occurred when heat advection due to shear heating and therefore  
330 shearing along the NBSASZ had stopped. Moreover, one cannot totally rule out the influence  
331 of some fluid-rock interactions which would have disturbed  $^{40}\text{Ar}/^{39}\text{Ar}$  age spectra without  
332 being recorded by the whole rock and muscovite chemistry. Indeed, the analyzed muscovite  
333 grains display subtle saddle-shaped  $^{40}\text{Ar}/^{39}\text{Ar}$  age spectra that may indicate fluid-induced  
334 disturbance (e.g. Alexandrov et al., 2002; Cheilietz et al., 1999). Finally, to a first order, our  
335 new data are consistent with a simple cooling of the intrusion, with possible, but limited,  
336 influence of shear heating and fluid-rock interaction. A surprising result is the absence of  
337 consistency between the muscovite  $^{40}\text{Ar}/^{39}\text{Ar}$  dates and the shearing gradients observe  
338 throughout the Lizio granite. This could result from the choice we made to date large  
339 muscovite phenocrysts in all the samples. It would deserve further studies, notably dating  
340 increasingly deformed micas toward the NBSASZ to better evaluate if potential post-  
341 emplacement events have affected the K-Ar system in micas.

342

## 343 **6. Conclusion**

344 Zircon U-Pb dating carried out on the Lizio granite yielded an age of  $316 \pm 6$  Ma that  
345 is interpreted as the emplacement age of the granite, and therefore also of dextral shearing  
346 along the northern branch of the South Armorican Shear Zone. This is significantly younger  
347 than the previous ca. 340 Ma whole rock Rb-Sr age interpreted as dating the emplacement of  
348 the Lizio granite. The significance of this older age is not yet well understood and it should  
349 therefore be treated with caution.  $^{40}\text{Ar}/^{39}\text{Ar}$  analyses performed on various muscovite grains

350 from the Lizio granite yielded dates of 311.5-308.2 Ma. As geochemical evidence precludes  
351 late fluids-induced large perturbations of the K-Ar isotopic system in muscovite, these dates  
352 likely reflect cooling ages below the argon closure temperature. Two extreme scenarios may  
353 explain the obtained ages, either a sub-instantaneous cooling of the granite or conversely a  
354 very slow cooling which lasted several millions of years. This last scenario requires that the  
355 Lizio granite remained in a hot environment for a long time after its emplacement. This could  
356 have been caused by shear heating due to dextral shearing along the northern branch of the  
357 South Armorican Shear Zone.

358

### 359 **Appendix A: 2D thermal numerical model**

360 The 2D thermal code used in this study solves the heat diffusion equation (A.1):

$$361 \quad \rho \cdot C_p \cdot \frac{\partial T}{\partial t} = k \cdot \nabla^2 T + Hr \quad (\text{A.1})$$

362 where  $\rho$ ,  $C_p$  and  $k$  are material density, specific heat capacity and thermal conductivity,  
363 respectively and  $Hr$  corresponds to the radiogenic heat production. This equation is solved  
364 numerically in the implicit formulation using the finite difference method. In this study, the  
365 heat production ( $Hr$ ) is set to zero. Indeed, preliminary tests have been done with values from  
366 1 to 5  $\mu\text{W}\cdot\text{m}^{-3}$  and the results show that results are not significantly different after 1Myr of  
367 experiment. The initial setup is displayed in the Fig. A1. The granitic intrusion is modelled as  
368 an ellipse (5 km high and 10 km long) located at 15 km depth in a host rocks medium with a  
369 linear thermal gradient of  $30^\circ\text{C}\cdot\text{km}^{-1}$ . The resolution used is 151 x 151 nodes (i.e., 200 m).

370

### 371 **Aknowledgments**

372 We are grateful to J. Tudri and O. Pourret (LaSalle Insitute, Beauvais, France) for providing  
373 us access to the secondary electron microprobe and to M. Bohn (IFREMER, Brest, France)

374 for his assistance during electron microprobe analyses. This work was funded by grants from  
375 the CNRS-INSU ( “3F” and “Action incitative” programs).

376

377

## 378 **References**

379 Alexandrov, P., Ruffet, G., Cheilletz, A., 2002. Muscovite recrystallization and saddle-shaped

380  $^{40}\text{Ar}/^{39}\text{Ar}$  age spectra: Example from the Blond granite (Massif Central, France).

381 *Geochim. Cosmochim. Ac.* 66, 1793-1807.

382 Ballèvre, M., Bosse, V., Ducassou, C., Pitra, P., 2009. Palaeozoic history of the Armorican

383 Massif: Models for the tectonic evolution of the suture zones. *C. R. Geosci.* 341, 174-

384 201.

385 Bea, F., Montero, P., González-Lodeiro, F., Talavera, C., 2007. Zircon inheritance reveals

386 exceptionally fast crustal magma generation processes in Central Iberia during the

387 Cambro-Ordovician. *J. Petrol* 48, 2327-2339.

388 Béchenec, F., Hallégouët, B., Thiéblemont, D., 2001. Rosporden 1/50000 geological map

389 manual (347). BRGM, Orléans, France.

390 Bernard-Griffiths, J., Peucat, J.J., Sheppard, S., Vidal, P., 1985. Petrogenesis of Hercynian

391 leucogranites from the Southern Armorican Massif: contribution of REE and isotopic (Sr,

392 Nd, Pb and O) geochemical data to the study of source rock characteristics and ages.

393 *Earth Planet. Sci. Lett.* 74, 235-250.

394 Berthé, D., 1980. Le Cisaillement Sud Armoricaïn dans la région de St. Jean Brévelay

395 (Morbihan). Analyse de la déformation cisailante. Unpublished Ph.D. Thesis, University

396 of Rennes 1, France.

397 Berthé, D., Choukroune, P., Jégouzo, P., 1979. Orthogneiss, mylonite and non coaxial  
398 deformation of granites - Example of the South Armorican Shear Zone. *J. Struct. Geol.* 1,  
399 31-42.

400 Brown, M., Dallmeyer R.D., 1996. Rapid Variscan exhumation and the role of magma in core  
401 complex formation: southern Brittany metamorphic belt, France. *J. Metamorph. Geol.* 14,  
402 361-379.

403 Cheilletz, A., Ruffet, G., Marignac, C., Kolli, O., Gasquet, D., Féraud, G., Bouillin, J.P.,  
404 1999.  $^{40}\text{Ar}/^{39}\text{Ar}$  dating of shear zones in the Variscan basement of the Greater Kabylia  
405 (Algeria). Evidence of an Eo-Alpine event at 128 Ma (Hauterivian–Barremian boundary):  
406 geodynamic consequences. *Tectonophysics* 306, 97-116.

407 Cherniak, D.J., Watson, E.B., 2001. Pb diffusion in zircon. *Chem. Geol.* 172, 5-24.

408 Gapais, D. 1989. Shear structures within deformed granites: mechanical and thermal  
409 indicators. *Geology* 17, 1144-1147.

410 Gapais, D., Lagarde, J.L., Le Corre, C., Audren, C., Jégouzo, P., Casas Sainz, A., Van Den  
411 Driessche, J., 1993. La zone de cisaillement de Quiberon : témoin d'extension de la  
412 chaîne varisque en Bretagne méridionale au Carbonifère. *C. R. Acad. Sci. II A* 316, 1123-  
413 1129.

414 Gloaguen, E., Branquet, Y., Boulvais, P., Moëlo, Y., Chauvel, J.J., Chiappero, P.J., Marcoux,  
415 E., 2007. Palaeozoic oolitic ironstone of the French Armorican Massif: a chemical and  
416 structural trap for orogenic base metal-As-Sb-Au mineralisation during Hercynian strike-  
417 slip deformation. *Miner. Deposita* 42, 399-422.

418 Gumiaux, C., Gapais, D., Brun, J.P., Chantraine, J., Ruffet, G., 2004. Tectonic history of the  
419 Hercynian Armorican Shear belt (Brittany, France). *Geodin. Acta* 17, 289-307.

420 Harrison, T.M., Aleinikoff, J.N., Compston, W., 1987. Observations and controls on the  
421 occurrence of inherited zircon in Concord-type granitoids, New Hampshire. *Geochim.*  
422 *Cosmochim. Ac.* 51, 2549-2558.

423 Harrison, T.M., Célérier, J., Aikman, A.B., Hermann, J., Heizler, M.T., 2009. Diffusion of  
424 <sup>40</sup>Ar in muscovite. *Geochim. Cosmochim. Ac.* 73, 1039-1051.

425 Jackson, S.E., Pearson, N.J., Griffin, W.L., Belousova, E.A., 2004. The application of laser  
426 ablation-inductively coupled plasma-mass spectrometry to in situ U-Pb zircon  
427 geochronology. *Chem. Geol.* 211, 47-69.

428 Jégouzo, P., 1980. The South Armorican Shear Zone. *J. Struct. Geol.* 2, 39-47.

429 Jégouzo, P., Rossello, E.A., 1988. La Branche Nord du Cisaillement Sud–Armoricain  
430 (France): un essai d'évaluation du déplacement par l'analyse des mylonites. *C. R. Acad.*  
431 *Sci. II A* 307, 1825-1831.

432 Košler, J., Sylvester, P.J., 2003. Present trends and the future of zircon in geochronology:  
433 laser ablation ICPMS. In: Hanchar, J.M., Hoskin, P.W.O. (Eds.), *Zircon. Rev. Mineral.*  
434 *Geochem.* 53, 243-275.

435 Košler, J., Fonneland, H., Sylvester, P., Tubrett, M., Pedersen, R.B., 2002. U-Pb dating of  
436 detrital zircons for sediments provenance studies – a comparison of laser ablation ICPMS  
437 and SIMS techniques. *Chem. Geol.* 182, 605-618.

438 Košler, J., Forst, L., Sláma, J., 2008. Lamdate and Lamtool: spreadsheet-based data reduction  
439 for laser ablation ICP-MS. In: Sylvester, P. (Ed.), *Laser Ablation ICP-MS in the Earth*  
440 *Sciences: Current Practices and Outstanding Issues. Mineralogical Association of*  
441 *Canada, Short Course Series* 40, 315-317.

442 Le Corre, C., Auvray, B., Ballèvre, M., Robardet, M., 1991. Le Massif Armoricain. *Sciences*  
443 *Géologiques* 44, 31-103.

444 Leloup, P.H., Ricard, Y., Battaglia, J., Lacassin, R., 1999. Shear heating in continental strike-  
445 slip shear zones: model and field examples. *Geophys. J. Int.* 136, 19-40.

446 Lemarchand, J., Boulvais, P., Gaboriau, M., Boiron, M.C., Tartèse, R., Cokkinos, M., Bonnet,  
447 S., Jégouzo, P., 2011. Giant quartz vein formation and high elevation meteoric fluid  
448 infiltration into the South Armorican Shear Zone: geological, fluid inclusion and stable  
449 isotope evidence. *J. Geol. Soc. London*, in press. doi: 10.1144/0016-76492010-186.

450 Ludwig, K.R., 2008. Isoplot/Ex version 3.70: A geochronological toolkit for Microsoft Excel.  
451 Berkeley Geochronology Center, Special Publication 4, 73 pp.

452 Miller, C.F., Stoddard, E.F., Bradfish, L.J., Dollase, W.A., 1981. Composition of plutonic  
453 muscovite; genetic implications. *Can. Mineral.* 19, 25-34.

454 Miller, C.F., McDowell, S.M., Mapes, R.W., 2003. Hot and cold granites? Implications of  
455 zircon saturation temperatures and preservation of inheritance. *Geology* 31, 529-532.

456 Pattison, D.R.M., Tracy, R.J., 1991. Phase equilibria and thermobarometry of metapelites. In:  
457 Kerrich, D.M. (Ed.), *Contact Metamorphism. Rev. Mineral. Geochem.* 26, 105-206.

458 Pattison, D.R.M., Spear, F.S., Cheney, J.T., 1999. Polymetamorphic origin of muscovite +  
459 cordierite + staurolite + biotite assemblages: implications for the metapelitic petrogenetic  
460 grid and for P-T paths. *J. Metamorph. Geol.* 17, 685-703.

461 Peucat, J.J., Charlot, R., Mifdal, A., Chantraine, J., Autran, A., 1979. Définition  
462 géochronologique de la phase bretonne en Bretagne centrale. Etude Rb/Sr de granites du  
463 domaine centre armoricain. *Bull. B.R.G.M.* 4, 349-356.

464 Pitra, P., Boulvais, P., Antonoff, V., Diot, H., 2008. Wagnerite in a cordierite-gedrite gneiss:  
465 witness of long-term fluid-rock interaction in the continental crust (Ile d'Yeu, Armorican  
466 Massif, France). *Am. Mineral.* 93, 315-326.

467 Purdy, J.W., Jäger, E., 1976. K-Ar ages on rock-forming minerals from the Central Alps.  
468 *Mem. Inst. Geol. Min. Univ. Padova*, 30.

469 Renne P.R., Swisher, C.C., Deino, A.L., Karner, D.B., Owens, T.L., DePaolo, D.J., 1998.  
470 Intercalibration of standards, absolute ages and uncertainties in  $^{40}\text{Ar}/^{39}\text{Ar}$  dating. *Chem.*  
471 *Geol.* 145, 117-152.

472 Roddick, J.C., Bevier, M.L., 1995. U-Pb dating of granites with inherited zircon:  
473 Conventional and ion microprobe results from two Paleozoic plutons, Canadian  
474 Appalachians. *Chem. Geol.* 119, 307-329.

475 Roddick, J.C., Compston, W., 1977. Strontium isotopic equilibration: A solution to a paradox.  
476 *Earth Planet. Sci. Lett.* 34, 238-246.

477 Ruffet, G., Féraud, G., Amouric, M., 1991. Comparison of  $^{40}\text{Ar}/^{39}\text{Ar}$  conventional and laser  
478 dating of biotites from the North Tregor batholiths. *Geochim. Cosmochim. Ac.* 55, 1675-  
479 1688.

480 Ruffet, G., Féraud, G., Ballèvre, M., Kienast, J.R., 1995. Plateau ages and excess argon in  
481 phengites - An Ar-40-Ar-39 laser probe study of alpine micas (Sesia zone, Western Alps,  
482 northern Italy). *Chem. Geol.* 121, 327-343.

483 Sláma, J., Košler, J., Condon, D.J., Crowley, J.L., Gerdes, A., Hanchar, J.M., Horstwood,  
484 M.S.A., Morris, G.A., Nasdala, L., Norberg, N., Schaltegger, U., Schoene, B., Tubrett,  
485 M.N., Whitehouse, M.J., 2008. Plešovice zircon - a new natural reference material for U-  
486 Pb and Hf isotopic microanalysis. *Chem. Geol.* 249, 1-35.

487 Tartèse, R., Boulvais, P., 2010. Differentiation of peraluminous leucogranites "en route" to  
488 the surface. *Lithos* 114, 353-368.

489 Tartèse, R., Boulvais, P., Poujol, M., Chevalier, T., Paquette, J. L., Ireland, T.R., Deloule, E.,  
490 2011a. Mylonites of the South Armorican Shear Zone: Insights for crustal-scale fluid  
491 flow and water-rock interaction processes. *J. Geodyn.*, in press. doi:  
492 10.1016/j.jog.2011.05.003.

493 Tartèse, R., Boulvais, P., Poujol, M., Gloaguen, E., 2011b. The late Carboniferous Variscan  
494 evolution of the Armorican Massif (France): magmatism, hydrothermalism and  
495 metallogenic consequences. *Geophys. Res. Abstr.* 13, 2422.

496 Turrillot, P., Augier, R., Faure, M., 2009. The top-to-the-southeast Sarzeau shear zone and its  
497 place in the late-orogenic extensional tectonics of southern Armorica. *Bull. Soc. Géol. Fr.*  
498 180, 247-261.

499 Villa, I.M., 2010. Disequilibrium textures versus equilibrium modelling: geochronology at the  
500 crossroads. In: Spalla, M.I., Marotta, A.M., Grosso, G. (Eds.), *Advances in Interpretation*  
501 *of Geological Processes: Refinement of Multi-scale Data and Integration in Numerical*  
502 *Modelling.* Geol. Soc. London Spec. Pub. 332, 1-15.

503 Wiedenbeck, M., Alle, P., Corfu, F., Griffin, W.L., Meier, M., Oberli, F., von Quadt, A.,  
504 Roddick, J.C., Spiegel, W., 1995. Three natural zircon standards for U-Th-Pb, Lu-Hf,  
505 trace element and REE analyses. *Geostandard. Newslett.* 19, 1-23.

506 Whitney, D.L., Evans, B.W., 2010. Abbreviations for names of rock-forming minerals. *Am.*  
507 *Mineral.* 95, 185-187.

508

509

510 **Table caption**

511 Table 1: Average chemical compositions of muscovite.

512

513 Table 2: Zircon U-Pb isotopic data. All uncertainties are at  $1\sigma$ .

514

515 **Figure caption**

516 Fig. 1: a) Location of the studied area in the Armorican Massif. NASZ: North Armorican

517 Shear Zone; SASZ: South Armorican Shear Zone. b) Simplified geological map of the studied

518 area showing the plutonic intrusions. NBSASZ and SBSASZ are the northern and southern  
519 branches of the South Armorican Shear Zone, respectively. P, B and L are the Pontivy,  
520 Bignan and Lizio granites, respectively. CAD and SAD are the central and south Armorican  
521 domains, respectively.

522

523 Fig. 2: Simplified geological map of the Lizio granite (after Berthé, 1980).

524

525 Fig. 3: Photomicrographs showing the typical structures of the Lizio granite samples, from  
526 undeformed (a and b) to mylonitized (c and d). Mineral abbreviations are after Whitney and  
527 Evans (2010).

528

529 Fig. 4: a) Muscovite chemical compositions plotted in the ternary Mg-Ti-Na diagram of  
530 Miller et al. (1981). b) Mg+Fe (apfu) vs. Si (apfu) content of muscovite showing the extent of  
531 phengitic substitution.

532

533 Fig. 5: a) Wetherill concordia diagram for zircon data from the sample LRT10. b) Wetherill  
534 concordia diagram for zircon data from the sample LRT15. c) Wetherill concordia diagram  
535 for zircon data from the sample LRT12. In these diagrams, error ellipses are at  $1\sigma$ . Concordia  
536 ages have been calculated with the ellipses in grey and include decay constants errors. d)  
537 SEM BSE images of zircon grains from samples LRT12 and LRT15 with LA-ICP-MS  
538 analyzed rasters (dotted zones) and obtained  $^{206}\text{Pb}/^{238}\text{U}$  dates. For all the grains, the scale bar  
539 represents 50  $\mu\text{m}$ .

540

541 Fig. 6:  $^{40}\text{Ar}/^{39}\text{Ar}$  age spectra of analyzed muscovites. The age error bars for each temperature  
542 steps are at the  $1\sigma$  level. The errors in the J-values are not included. Plateau ages are given  
543 with a  $2\sigma$  uncertainty.

544

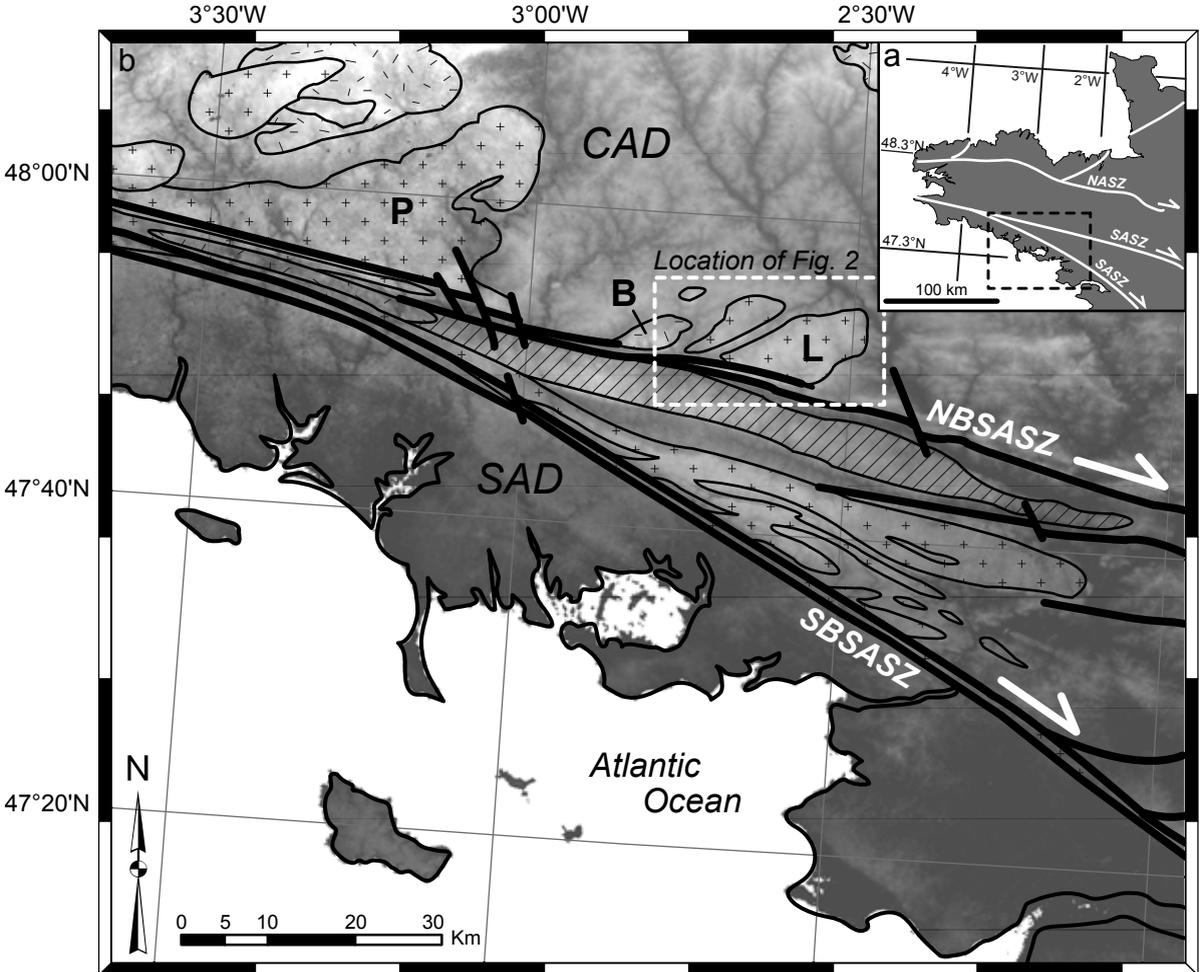
545 Fig. 7: a) Computation of muscovite closure temperature ( $^{\circ}\text{C}$ ) for Ar diffusion against the  
546 cooling rate ( $^{\circ}\text{C}/\text{Ma}$ ) for diffusion radius of 0.5 and 1 mm. Parameters used are those of  
547 Harrison et al. (2009). b) Temperature-Time plot for the Lizio granite.

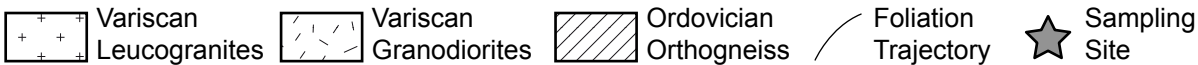
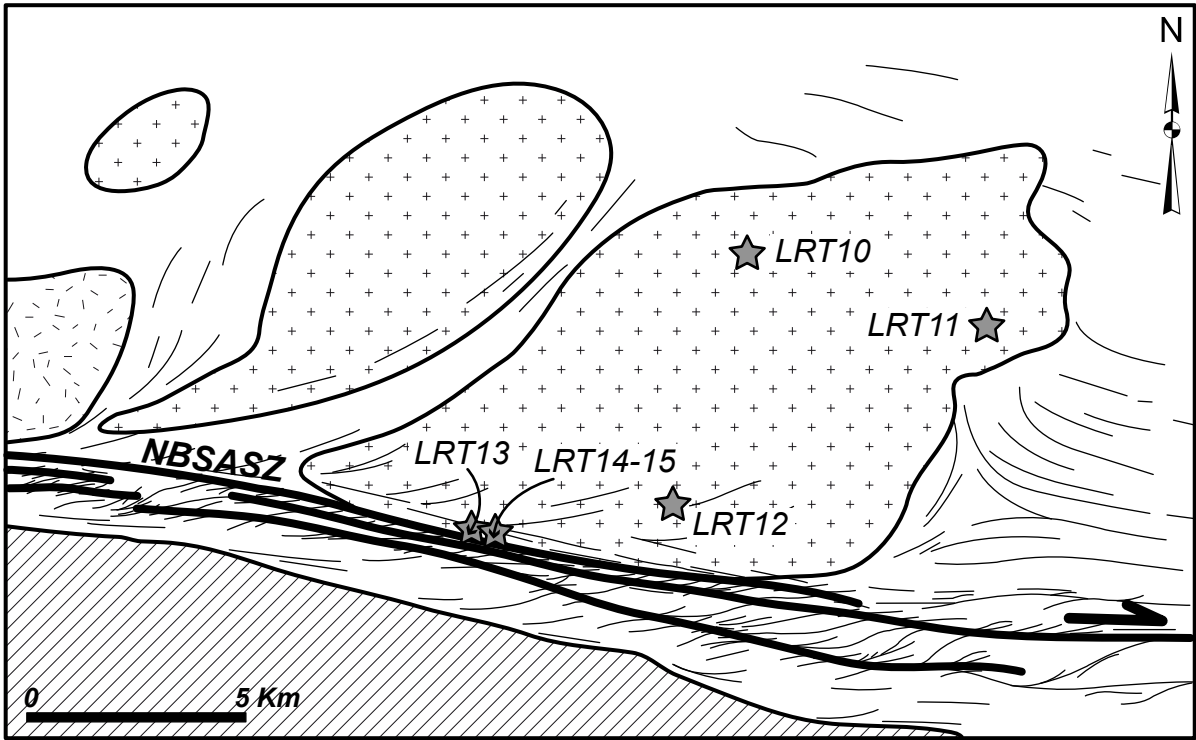
548

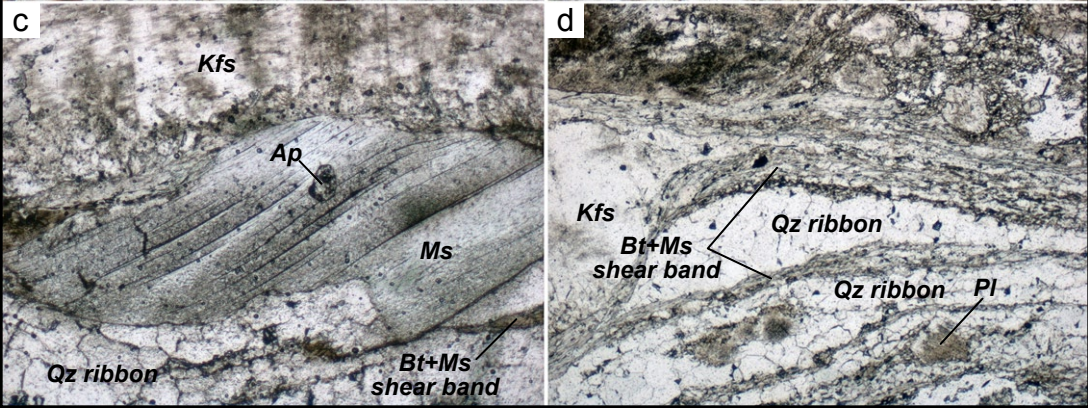
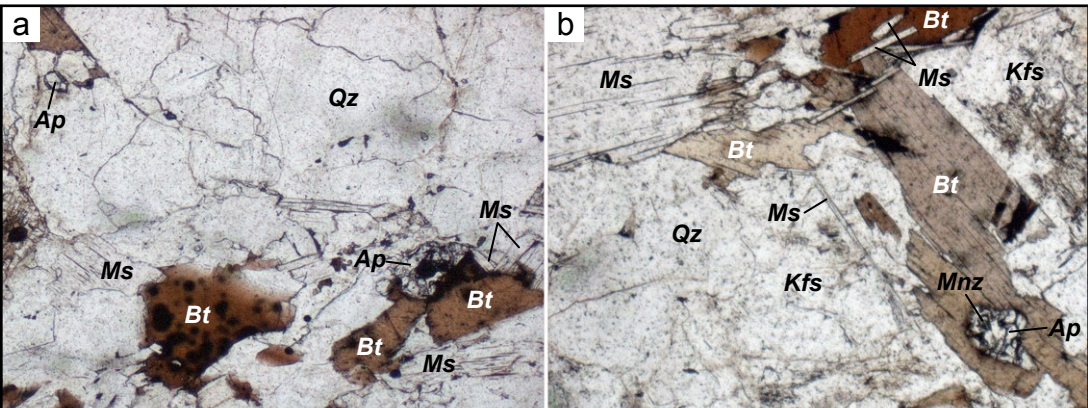
549 Fig. 8: 2D thermal modelling of the cooling of the Lizio granite during 1 Ma (see details in  
550 Appendix A).

551

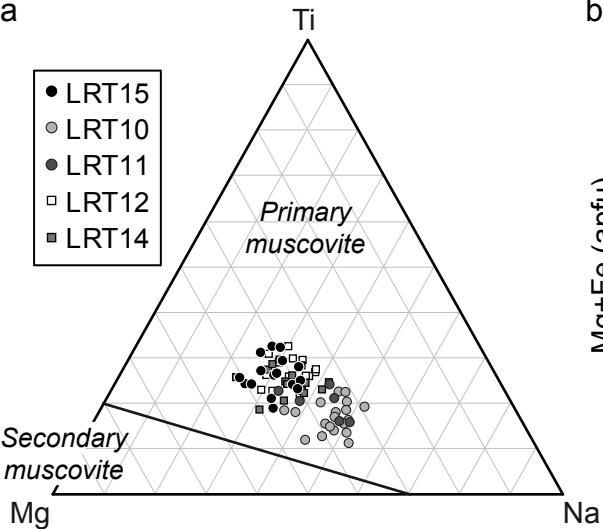
552 Fig. A1: Initial setup used for the 2D thermal modelling.



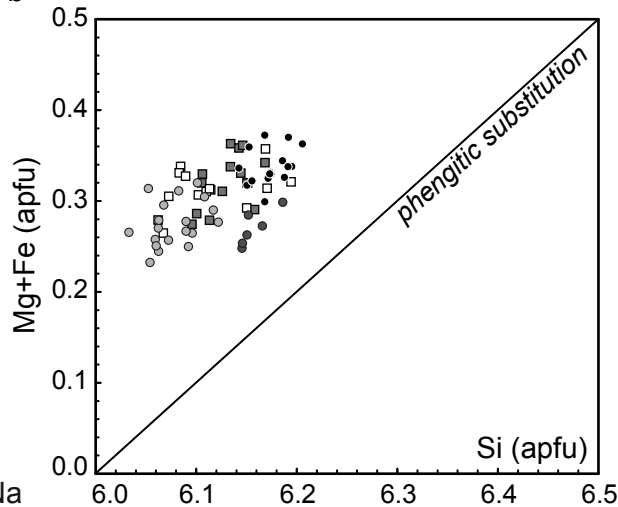


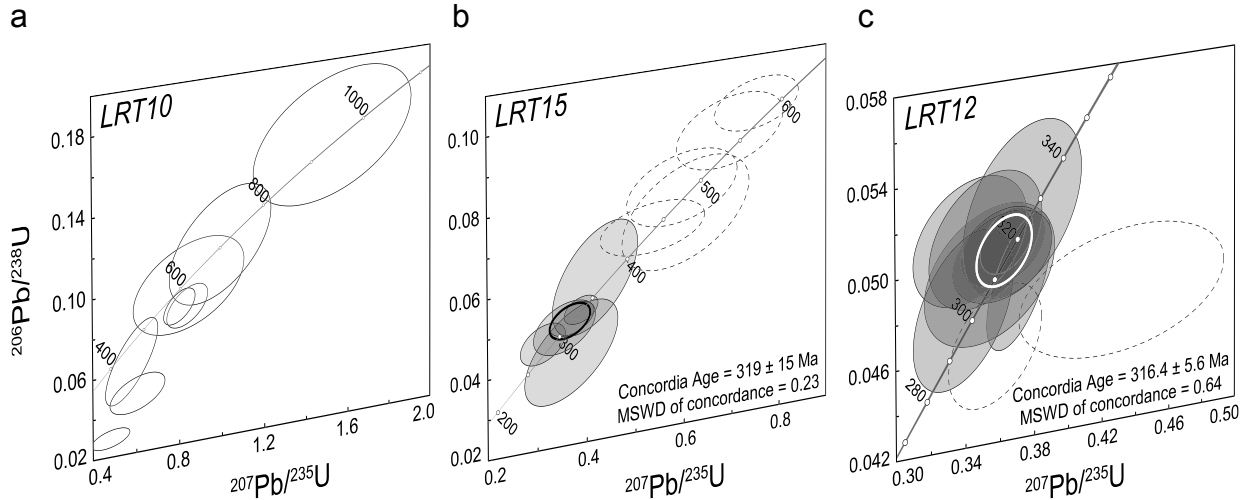


a

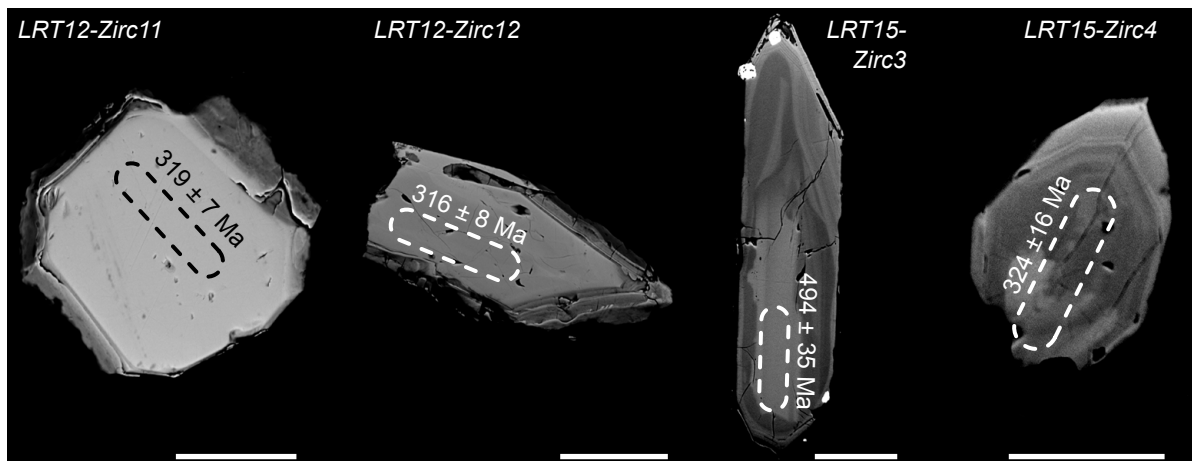


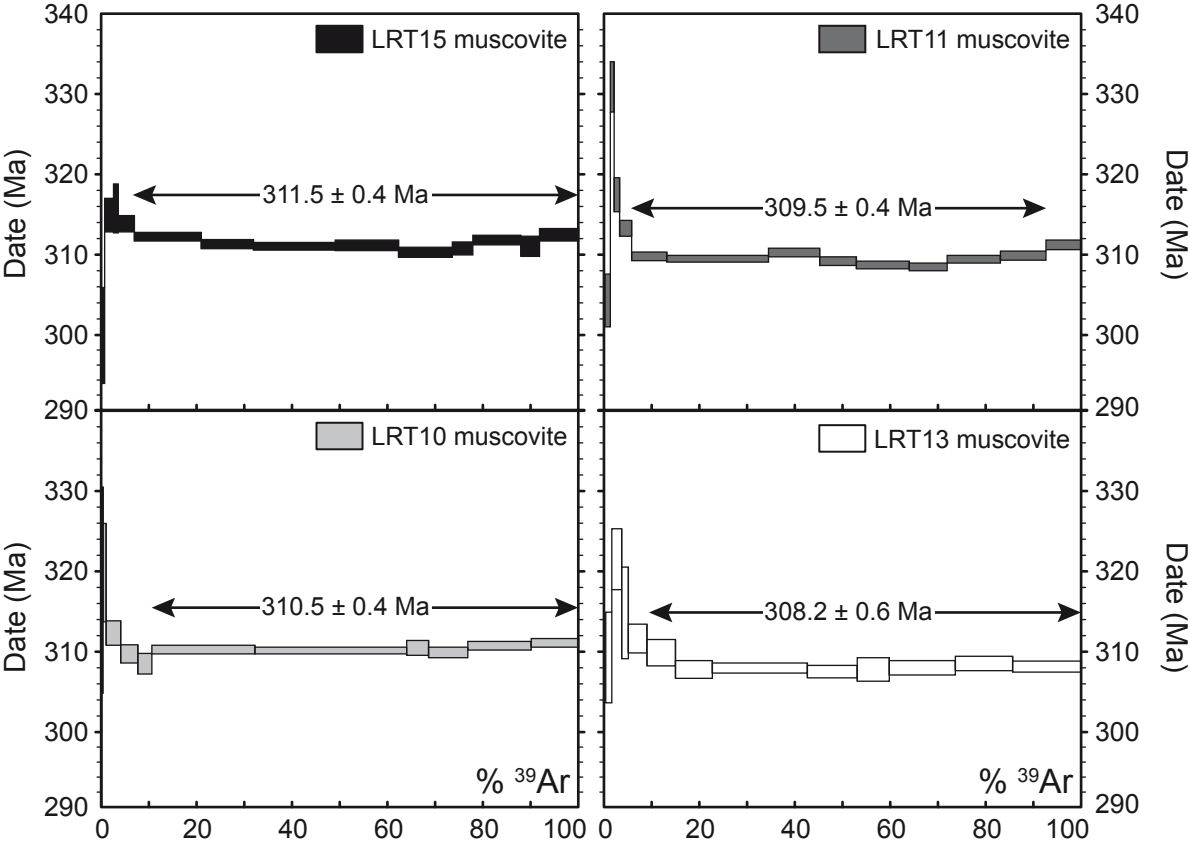
b



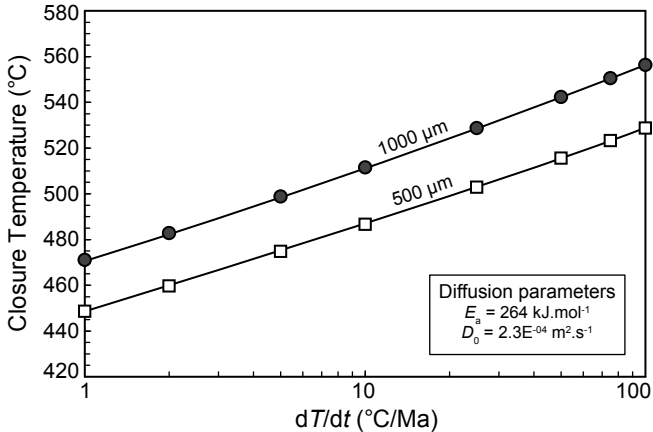


**d**

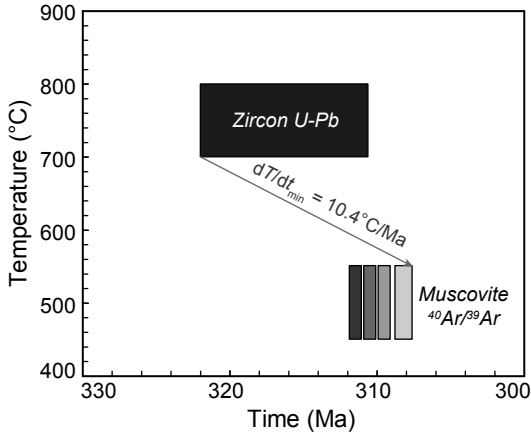


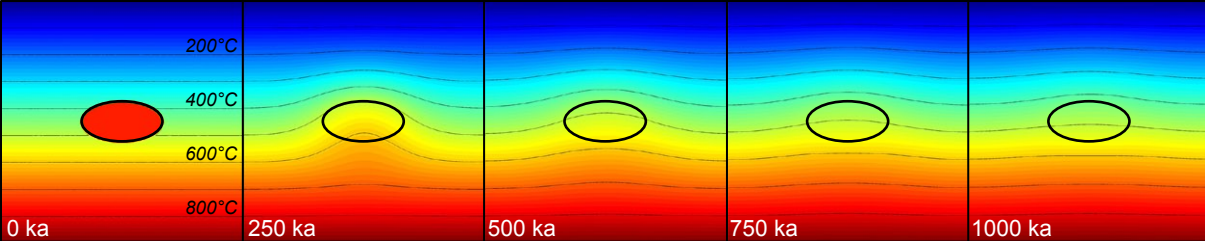


a

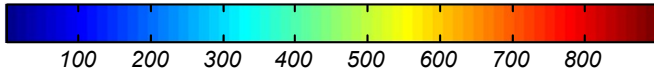


b





Temperature ( $^{\circ}\text{C}$ )



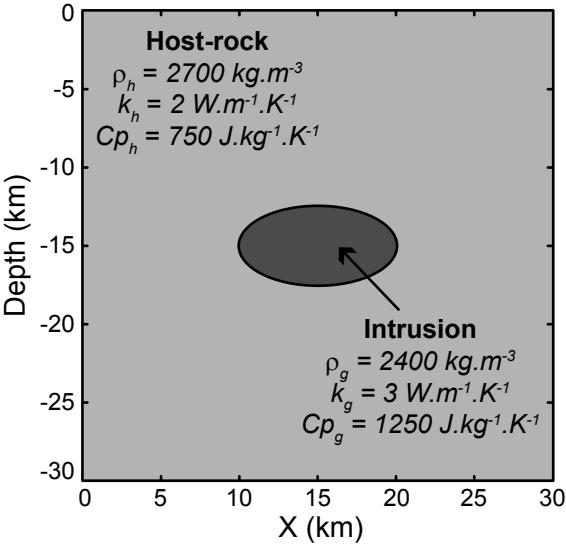


Table 1: Average chemical compositions of muscovite.

<b>MUSCOVITE</b>										
	LRT15 (n=16)	sd	LRT10 (n=19)	sd	LRT11 (n=10)	sd	LRT12 (n=14)	sd	LRT14 (n=15)	sd
SiO <sub>2</sub>	46.5	0.3	45.7	0.4	46.4	0.2	45.7	0.5	46.1	0.3
TiO <sub>2</sub>	1.1	0.2	0.7	0.2	0.6	0.2	1.1	0.2	1.0	0.2
Al <sub>2</sub> O <sub>3</sub>	34.5	0.2	35.8	0.3	35.0	0.3	34.7	0.5	34.9	0.4
FeO	1.4	0.1	1.1	0.1	1.2	0.2	1.3	0.1	1.4	0.1
MgO	0.9	0.1	0.8	0.1	0.8	0.1	0.8	0.1	0.8	0.1
Na <sub>2</sub> O	0.5	0.1	0.7	0.1	0.6	0.1	0.5	0.1	0.5	0.1
K <sub>2</sub> O	11.0	0.2	10.8	0.2	10.7	0.6	11.2	0.3	11.1	0.2
SUM	95.8		95.6		95.3		95.4		95.8	
Structural formula based on 22 oxygen atoms										
Si	6.17	0.02	6.08	0.02	6.17	0.03	6.11	0.04	6.13	0.02
Ti	0.11	0.02	0.07	0.02	0.06	0.02	0.11	0.02	0.10	0.02
Al	5.40	0.03	5.61	0.03	5.49	0.03	5.48	0.06	5.47	0.05
Fe	0.16	0.01	0.13	0.01	0.14	0.02	0.15	0.01	0.15	0.01
Mg	0.18	0.01	0.15	0.01	0.15	0.02	0.16	0.02	0.17	0.02
Na	0.12	0.02	0.19	0.03	0.15	0.04	0.14	0.03	0.14	0.03
K	1.86	0.04	1.84	0.04	1.83	0.09	1.91	0.04	1.88	0.03
SUM	14.00		14.06		13.99		14.06		14.04	

*Oxide contents in wt.% and cationic contents in apfu.*

*sd = Standard deviation*

Table 2: Zircon U-Pb isotopic data. All uncertainties are at  $1\sigma$

Sample, grain, spot	Isotopic ratios						Rho	Calculated ages (Ma)					
	$^{207}\text{Pb}/^{235}\text{U}$	$\pm$	$^{206}\text{Pb}/^{238}\text{U}$	$\pm$	$^{207}\text{Pb}/^{206}\text{Pb}$	$\pm$		$^{206}\text{Pb}/^{238}\text{U}$	$\pm$	$^{207}\text{Pb}/^{235}\text{U}$	$\pm$	$^{207}\text{Pb}/^{206}\text{Pb}$	$\pm$
<i>LRT10 - Zircon</i>													
Zirc1.2	0.8456	0.1709	0.0986	0.0150	0.0618	0.0063	0.38	606	88	622	94	667	220
Zirc2.1	1.5298	0.2502	0.1619	0.0217	0.0695	0.0065	0.41	967	120	942	100	915	192
Zirc3.1	0.8374	0.0634	0.0885	0.0067	0.0729	0.0084	0.50	547	40	618	35	1011	233
Zirc4.1	0.5790	0.0799	0.0656	0.0134	0.0634	0.0082	0.74	410	81	464	51	723	275
Zirc5.1	0.9942	0.1581	0.1165	0.0185	0.0581	0.0065	0.50	710	107	701	81	532	245
Zirc7.1	0.6049	0.0842	0.0494	0.0061	0.0891	0.0086	0.45	311	38	480	53	1406	184
Zirc7.2	0.8016	0.0485	0.0889	0.0057	0.0612	0.0031	0.53	549	33	598	27	645	107
Zirc8.1	0.4803	0.0583	0.0290	0.0031	0.1430	0.0120	0.44	184	19	398	40	2264	145
<i>LRT12 - Zircon</i>													
Zirc2.1	0.4324	0.0406	0.0478	0.0019	0.0664	0.0051	0.21	301	11	365	29	819	159
Zirc4.1	0.3640	0.0102	0.0509	0.0009	0.0507	0.0014	0.33	320	6	315	8	227	65
Zirc5.1	0.3711	0.0125	0.0490	0.0019	0.0538	0.0015	0.59	308	12	320	9	363	62
Zirc6.1	0.3542	0.0251	0.0495	0.0020	0.0528	0.0032	0.29	312	12	308	19	320	138
Zirc7.1	0.3429	0.0219	0.0511	0.0018	0.0501	0.0021	0.28	322	11	299	17	198	100
Zirc8.1	0.3519	0.0218	0.0511	0.0019	0.0503	0.0022	0.31	321	12	306	16	211	102
Zirc8.2	0.3734	0.0230	0.0522	0.0025	0.0527	0.0022	0.39	328	15	322	17	315	93
Zirc9.1	0.3571	0.0179	0.0463	0.0018	0.0562	0.0026	0.38	292	11	310	13	460	102
Zirc11.1	0.3618	0.0162	0.0507	0.0011	0.0524	0.0023	0.25	319	7	314	12	302	101
Zirc12.1	0.3616	0.0191	0.0502	0.0013	0.0540	0.0022	0.24	316	8	313	14	373	91
Zirc13.1	0.3387	0.0192	0.0481	0.0023	0.0524	0.0016	0.42	303	14	296	15	303	71
<i>LRT15 - Zircon</i>													
Zirc1.1	0.4161	0.0578	0.0607	0.0090	0.0516	0.0056	0.53	380	54	353	41	268	250
Zirc2.1	0.3675	0.0629	0.0431	0.0080	0.0608	0.0096	0.54	272	50	318	47	634	338
Zirc3.1	0.5965	0.0759	0.0796	0.0059	0.0548	0.0039	0.29	494	35	475	48	405	161
Zirc3.2	0.6041	0.0876	0.0732	0.0088	0.0598	0.0077	0.42	455	53	480	55	596	280
Zirc4.1	0.3682	0.0297	0.0515	0.0026	0.0515	0.0034	0.32	324	16	318	22	262	153
Zirc5.1	0.3531	0.0417	0.0496	0.0042	0.0524	0.0054	0.36	312	26	307	31	304	237
Zirc5.2	0.3871	0.0229	0.0533	0.0022	0.0537	0.0026	0.35	335	13	332	17	357	111
Zirc6.1	0.7527	0.0583	0.0977	0.0042	0.0589	0.0021	0.28	601	25	570	34	564	79
Zirc7.1	0.5352	0.0713	0.0707	0.0041	0.0581	0.0054	0.22	440	25	435	47	533	204
Zirc8.1	0.3093	0.0302	0.0464	0.0032	0.0502	0.0025	0.36	292	20	274	23	204	115
Zirc9.1	0.6964	0.0739	0.0918	0.0059	0.0555	0.0031	0.30	566	35	537	44	432	125